Soft Matter

PAPER

View Article Online
View Journal | View Issue

Cite this: *Soft Matter*, 2016, 12, 3877

Structure of lipid multilayers *via* drop casting of aqueous liposome dispersions†

Beatrice Sironi,[a] Tim Snow,[a] Christian Redeker,[a] Anna Slastanova,[a] Oier Bikondoa,[bc] Thomas Arnold,[d] Jacob Klein[e] and Wuge H. Briscoe*[a]

Understanding the structure of solid supported lipid multilayers is crucial to their application as a platform for novel materials. Conventionally, they are prepared from drop casting or spin coating of lipids dissolved in organic solvents, and lipid multilayers prepared from aqueous media and their structural characterisation have not been reported previously, due to their extremely low lipid solubility (*i.e.* $\sim 10^{-9}$ M) in water. Herein, using X-ray reflectivity (XRR) facilitated by a "bending mica" method, we have studied the structural characteristics of dioleoylphosphatidylcholine (DOPC) multilayers prepared *via* drop casting aqueous small unilamellar and multilamellar vesicle or liposome (*i.e.* SUV and MLV) dispersions on different surfaces, including mica, positively charged polyethylenimine (PEI) coated mica, and stearic trimethylammonium iodide (STAI) coated mica which exposes a monolayer of hydrocarbon tails. We suggest that DOPC liposomes served both as a delivery matrix where an appreciable lipid concentration in water ($\sim$25 mg mL^{-1} or 14 mM) was feasible, and as a structural precursor where the lamellar structure was readily retained on the rupture of the vesicles at the solid surface upon solvent evaporation to facilitate rapid multilayer formation. We find that multilayers on mica from MLVs exhibited polymorphism, whereas the SUV multilayers were well ordered and showed stronger stability against water. The influence of substrate chemistry (*i.e.* polymer coating, charge and hydrophobicity) on the multilayer structure is discussed in terms of lipid–substrate molecular interactions determining the bilayer packing proximal to the solid–liquid interface, which then had a templating effect on the structure of the bilayers distal from the interface, resulting in the overall different multilayer structural characteristics on different substrates. Such a fundamental understanding of the correlation between the physical parameters that characterise liposomes and substrate chemistry, and the structure of lipid multilayers underpins the potential development of a simple method *via* an aqueous liposome dispersion route for the inclusion of hydrophilic functional additives (*e.g.* drugs or nanoparticles) into lipid multilayer based hybrid materials, where tailored structural characteristics are an important consideration.

Received 12th February 2016,
Accepted 14th March 2016

DOI: 10.1039/c6sm00369a

www.rsc.org/softmatter

1. Introduction

Lipid bilayers have been widely studied since Mueller's description of the classic black lipid membrane (BLM) in 1960s[1] and Tamm and McConnell's report on supported lipid bilayers (SLBs) in 1980s.[2] Using SLBs as model membranes,[3] biological processes at the cellular level, such as viral attack,[4,5] cellular signalling events[6,7] and ligand–receptor interactions[8–11] have been investigated. In addition, SLBs have found use in many applications, *e.g.* microcontact printing[12,13] and photolithography[14] to produce biofunctional nanomaterials such as label free biosensors, and several reviews exist on these topics.[15–17]

Using lipid bilayers as building units, lipid multilayers have also been prepared in which tens to thousands of bilayers can be stacked forming ordered structures. Phosphatidylcholine lipids have been widely used, as they are the main component of cell membranes. Various applications using lipid multilayers have been developed mainly in biology[18–20] and nanotechnology,[21,22] as model membranes to study their interactions with drugs and nanoparticles, and also as a platform for functional materials. For example, dioleoylphosphatidylcholine (DOPC) lipid multilayers with thicknesses between 5 and 100 nm on silicon wafers, glass,

---

[a] *School of Chemistry, University of Bristol, Cantock's Close, Bristol BS8 1TS, UK. E-mail: wuge.briscoe@bristol.ac.uk; Tel: +44 (0)117 3318256*
[b] *XMas, The UK-CRG Beamline, The European Synchrotron (ESRF), 71 Avenue des Martyrs, 38043 Grenoble, France*
[c] *Department of Physics, University of Warwick, Gibbet Hill Road, Coventry CV4 7AL, UK*
[d] *Diamond Light Source, Diamond House, Harwell Science and Innovation Campus, Didcot, Oxfordshire, OX11 0DE, UK*
[e] *Material and Interfaces Department, Weizmann Institute of Science, 76100 Rehovot, Israel*

† Electronic supplementary information (ESI) available. See DOI: 10.1039/c6sm00369a

evaporated metal films, polystyrene[22] and polymethyl methacrylate (PMMA)[21] substrates have been prepared by dip-pen nanolithography as photonic components. Similarly, DOPC, dioleoylphosphatidylethanolamine (DOPE), and dipalmitoylphosphatidylcholine (DPPC) gratings have been prepared on polydimethylsiloxane (PDMS) and glass, as potential biosensors for the detection of lipid–protein and lipid–drug interactions, and as a starting point for microarray development.[18–20] Lipid multilayers incorporating cholesterol- or sphingomyelin-enriched lipid multilayers on silica substrates have also been prepared for potential application in novel membrane-based functional materials and devices.[23]

Many studies have thus aimed to optimise lipid multilayer formation for enhanced structural order and stability. Whilst the most common method to prepare SLBs is to rupture liposomes on a substrate, the preparation of lipid multilayers on solid surfaces involves drop casting[24–30] or spin coating[31,32] from an organic solution of dissolved lipids (forming samples typically with thousands or tens of bilayers, respectively, for the drop- and spin-casting methods). In a series of studies, Salditt *et al.*[25,28,29,31–35] reported the formation of lipid multilayers by spin coating a lipid solution in an organic solvent onto silicon and glass substrates, showing that the number of stacked bilayers could be controlled by the volume and concentration of the solution and the spin speed. Dimyristoylphosphatidylcholine (DMPC) multilayers on silica were investigated by (X-ray reflectivity) XRR,[31] neutron reflectivity (NR),[32,34] atomic force microscopy (AFM), and optical microscopy.[32] XRR and NR profiles collected at temperatures above the lipid melting temperature, T_g, revealed single crystalline membranes with the stacking of at least 10 bilayers $\sim$5 nm in thickness. This correlated well with the step size of surface features revealed by AFM imaging. However, no features were observed with optical microscopy.

Tristan-Nagle[36] reported a ''rock and roll'' method to prepare multilayers, in which a lipid solvent solution was deposited on the substrate fixed on a vial that was rocked and rolled manually under controlled conditions. Different substrates (*i.e.* glass, mica, and silicon wafer) and lipids (*i.e.* phosphatidylcholine (PC), phosphatidylserine (PS) and phosphatidylethanolamine (PE) with different chain lengths) were investigated. AFM imaging suggested that the multilayers were more ordered than those obtained by spin coating. Similarly to the drop casting method, the ''rock and roll'' method produced multilayers comprising hundreds to thousands of bilayers.

A main drawback for lipid multilayers is their low stability, as they are unstable in the water-vapour atmosphere,[32] and can delaminate underwater thus losing their structural order.[37] Hydration of thick DOPC and dioleoyltrimetylammoniumpropane (DOTAP) multilayers ($\sim$1200 bilayers) prepared by drop casting on silicon wafer was found to lead to an increase of the lamellar spacing, *d*, as observed by electron density X-ray diffraction (EDXD).[24] Similar results were observed by Cavalcanti *et al.*,[26] when anticancer drugs were intercalated in lipid multilayers formed by DPPC and DOTAP. Multilayer unbinding can also be caused by heating[29] or by applying an electric field[25] to the lipid multilayer.

So far, all the lipid multilayer studies discussed have used organic solvents as the medium, as lipids dissolve in them readily at high concentrations (*e.g.* with concentrations of 2–20 mg mL^{-1} typically used), and the solvent can be easily evaporated after deposition. Dissolving a mixture of different lipids in an organic solvent also affords the possibility for the formation of mixed lipid multilayers.[27] It would be desirable, however, to develop an alternative route from an aqueous lipid dispersion, *e.g.* to facilitate a pathway for the inclusion of hydrophilic additives. However, lipid solubility in water is extremely low (with the solubility of biological lipids in the order of $\sim$nM), making the use of water as a solvent less straightforward, with very few related studies in the literature.

In the present work, DOPC lipid multilayers have been prepared by drop casting an aqueous liposome dispersion on different surfaces: negatively charged mica, positively charged PEI-coated mica, and STAI-coated mica, which exposes a monolayer of hydrocarbon tails making it more hydrophobic. The use of DOPC liposomes afforded an appreciable concentration of the lipid dispersion in water ($\sim$25 mg mL^{-1}), and also served as a structural precursor for subsequent multilayer formation during droplet evaporation. XRR was used to characterise the structure of the lipid multilayers, facilitated by a ''bending mica'' method.[38–40] Such XRR results on mica are unprecedented (and we note that neutron reflectivity has also been recently successfully applied to the mica surface[41]). The structures of multilayers obtained from dispersions of small unilamellar vesicles (SUVs) and multilamellar vesicles (MLVs) with different liposome sizes were compared. Polymorphism was observed in some samples, indicating the coexistence of bilayer domains with different *d*-spacing values. The influence of different substrate chemistries on the multilayer structure is discussed in terms of lipid–substrate molecular interactions affecting the bilayer packing at the interface. Our results on the structural characteristics of the DOPC multilayers *via* drop casting an aqueous liposome dispersion and their correlation between the physical parameters that characterise liposomes and substrate chemistry are of fundamental relevance and also offer a potential route to facilitate the incorporation of hydrophilic additives (*e.g.* drugs and nanoparticles) in lipid multilayer based hybrid materials.

2. Materials and methods

2.1. Materials and sample preparation

DOPC lipid (>99% purity, M_w = 786.113 g mol^{-1}) in chloroform (25 mg mL^{-1}) was purchased from Avanti® Polar Lipids, Alabaster, Alabama, and poly(ethyleneimine) (PEI; formula $(CH_2CH_2NH)_x$, M_w = 13 000 g mol^{-1}) from Polymer Source™, Quebec, Canada, both used with no further purification. Its main solid-ordered (SO) to liquid-disordered (LD) transition temperature is $T_m = -17$ °C, so that the lipid was in its LD phase at the temperature of the experiments. The stearic trimethylammonium iodide (STAI) surfactant, also known as octadecyltrimethylammonium iodide (formula $CH_3(CH_2)_{17}N^+(CH_3)_3I^-$), was prepared from octadecyltrimethylammonium chloride (STAC) as described in ref. 42 and also outlined in the ESI.† Natural muscovite mica ($KAl_2(Si_3Al)O_{10}(OH)_2$) of A1 special grade was purchased from SJ Trading®, New York. Ultrapure Milli-Q® water with a resistivity of 18.2 MΩ cm^{-1} and a total organic content (ToC) of 3–4 ppb at 25 °C, chloroform (VWR, ≥99.8% purity) and nitrogen (Air Liquide, oxygen free) were used for sample preparation and XRR measurements.

Mica surfaces were prepared, first by cutting an original sheet (of size ~25 cm × 15 cm × 1 mm) with a pair of precision scissors, and then by hand-cleaving, into smaller pieces. They were further cut into pieces of 3 × 1 cm in size and ~300 μm in thickness, as required for the XRR liquid cell.[39,43] STAI coated mica (*cf.* ESI†) was prepared by immersing a freshly cleaved mica piece into a 1 mg mL^{-1} aqueous STAI solution at 70 °C for 30 s, and this was followed by immersion in Milli-Q water at 70 °C for 30 s. The contact angle of a water droplet on such STAI-coated mica was ~71° (ESI†), indicating that it was more hydrophobic than bare mica. PEI-coated mica was prepared by dipping a freshly cleaved mica piece into a 100 ppm polymer solution for 10 min at room temperature (RT). The STAI- and PEI-coated surfaces were then left to dry in a laminar flow hood overnight, and all the surfaces were then kept in sealed glass vials to avoid any contamination, with the mica pieces positioned in such a way that only their bottom edge and top corners came into contact with the glass vial.

2.2. Preparation of lipid multilayers

A designated amount of DOPC in $CHCl_3$ (25 mg mL^{-1}) was weighed into a 7 mL glass vial, and the solvent was removed with a gentle N_2 stream to obtain a dried uniform crystal-free lipid film. The lipid film was first hydrated with Milli-Q water to a concentration of 14 mM and sonicated for 1/2 hour (h) at RT (above the DOPC melting temperature (T_m) of −17 °C). The obtained dispersion was gently shaken manually and then the size of the resultant liposomes was checked with dynamic light scattering (DLS), using a Malvern Nano Zetasiser ZS (Malvern Instruments, Malvern, Worcestershire, UK). DLS measurements revealed that a multilamellar vesicle (MLV) dispersion was obtained, containing a mixture of MLVs of ~150 nm in diameter, and bigger aggregates typically of size ~300–1500 nm, with a polydispersity index (PDI) of ~1. These results are consistent with previous reports.[44,45]

The MLV dispersion was then extruded through first 0.4 μm and then 0.1 μm pore size polycarbonate membranes (Avanti® Polar Lipids Inc., Alabaster, Alabama) 3 times each using a LIPEX™ 10 mL Thermobarrel Extruder (Northern Lipids Inc., Burnaby, Canada) under ~20 bar pressure of N_2 or 21 times each using a manual Avanti® Mini Extruder apparatus (Avanti® Polar Lipids Inc., Alabaster, Alabama). DLS measurements of the obtained dispersion showed that single lamellar vesicles or liposomes (SUVs) of diameter ~90 nm with a narrow size distribution (PDI = 0.05) were formed. For drop casting, both the SUV and MLV DOPC dispersions were diluted to 2 mg mL^{-1} with Milli-Q water, and 100 μL of each dispersion was dropped onto the substrate, with care taken to ensure that the droplet formed did not spill over the mica sheet. The samples were left to dry in a vacuum oven at RT for 2 h to ensure the removal of water, with a dried footprint of the thin film ~1 cm^2 in area and ~2 μm in thickness. The multilayers thus formed were kept in clean sealed vials at 4 °C until synchrotron X-ray reflectivity measurements were performed.

2.3. X-ray reflectivity (XRR) liquid cell and Synchrotron XRR measurements

The liquid cell used in the XRR measurements (Fig. 1) employs a ''bending mica'' method,[40] with a mica piece gently bent over an underlying cylindrical sample support of radius R = 7.5 cm and clamped *via* two small plates. This enhances the rigidity of mica along the bending axis, thus providing sufficient flatness for the XRR measurements along this axis. The liquid cell was described in detail elsewhere[43] (see ESI† for a brief description of the liquid cell and sample alignment).

XRR measurements were performed at beamline BM28 at the European Synchrotron Radiation Facility (ESRF), Grenoble, France, and also at beamline I07 at the Diamond Light Source (DLS), Didcot, UK. XRR measurements were typically made at

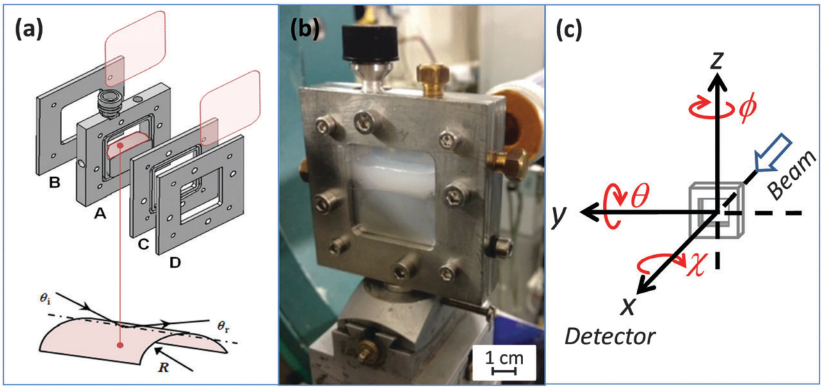

Fig. 1 (a) Schematic representation of the main components of the XRR liquid cell, consisting of four stainless steel plates (A–D) and a cylindrical stage on which a 3 × 1 cm mica is gently bent. XRR measurements are made along the rigidified bending axis. (b) A photograph of the XRR liquid cell as mounted on the goniometer at ESRF beamline BM28. The white/yellow scale bar in (b) is 1 cm. (c) Translational (x, y, and z) and rotational (θ, ϕ, and χ) axes of the Huber diffractometer with respect to the XRR cell (grey, schematic), beam, and detector. (*cf.* ESI† for details.)

room temperature for all the samples in air, then water was injected into the liquid cell and the measurement repeated, with an integration time of ∼1–5 seconds at each angle (*e.g.* in the range $\theta_i = 0.06°–2.6°$ corresponding to a Q range of ∼0.015 to 0.64 $Å^{-1}$ for $\lambda = 0.886$ Å at BM28) at a typical step size of 0.01°, where the momentum transfer vector normal to the sample surface is $Q = (4\pi\sin\theta_i)/\lambda$. The specularly reflected intensity was detected at each angle $\theta_r = 2\theta_i$ using an avalanche photodiode detector (APD) at ESRF BM28, and using a Pilatus 100 K 2D detector at Diamond Light Source I07. The resulting reflectivity curve can be plotted as reflectivity (a.u.) *versus* Q ($Å^{-1}$). Measurement details and sample alignment procedures are given in the ESI.†

3. Results and discussion

Fig. 2A shows an example XRR curve from a thin film sample drop cast from a DOPC MLV dispersion on bare mica. A distinct feature in the XRR curves for the DOPC multilayer thin films in air is the presence of sharp Bragg peaks up to the 4th order ($n = 4$) of diffraction (also Fig. 3A for an SUV sample), as compared to that of bare mica (*cf.* Fig. 5F). These peaks are attributed to the diffractions from the lattice planes of the highly ordered multilayers approximately parallel to the substrate, and the ratio of 1 : 2 : 3... in the peak positions Q_n (of order $n = 1, 2, 3...$) is consistent with a lamellar structure. The *d*-spacing, which is the lipid bilayer thickness or the periodic distance between the lamellar lattice spacing, can be calculated as

$$d = \frac{2n\pi}{Q_n}, \tag{1}$$

yielding $d \sim 46.8–50.6$ Å (±0.2 Å) (Table 1; MLVs), which is consistent with a DOPC bilayer thickness.[24] The error analysis details are given in the ESI.† The overall shape of the curve results from the morphological surface characteristics (*i.e.* coverage, relaxation of the upper layer, roughness), and a detailed structural model incorporating these features is presented elsewhere.[46] At $Q = 0.6$ $Å^{-1}$ the reflectivity from all the samples starts to

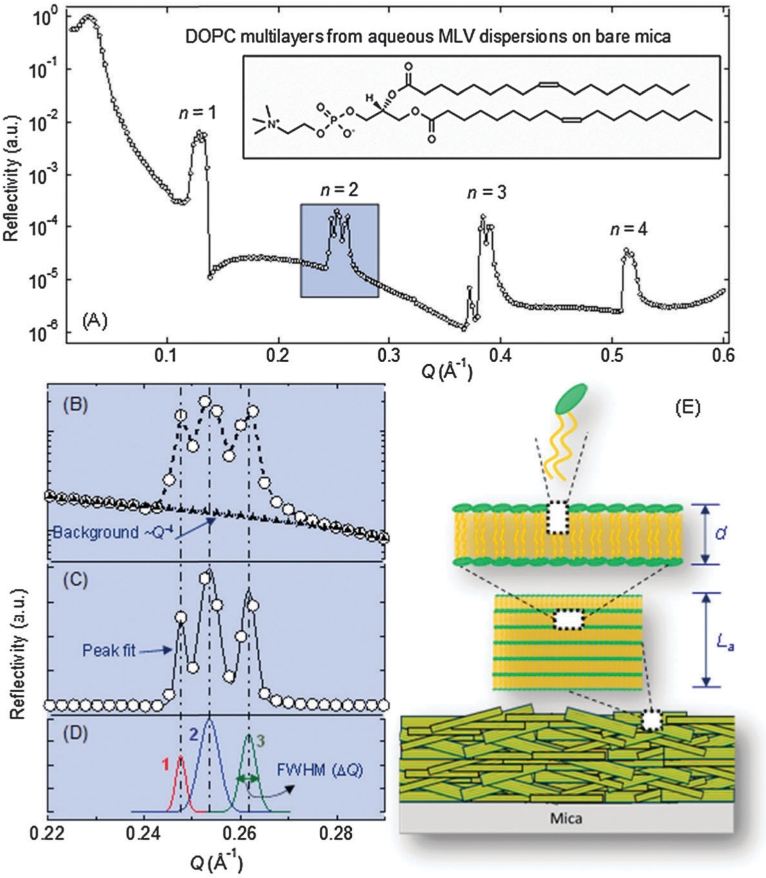

Fig. 2 (A) Experimental XRR curve of the DOPC multilayer from an MLV dispersion on bare mica, collected in air at room temperature. (B) An enlarged view of the reflectivity on a log-linear scale around the second order ($n = 2$) Bragg peak (as enclosed in the rectangle in (A)), with the background fitted to Q^{-4}. (C) The residual peak after background subtraction (circles), and its fit (black curve) calculated using the IGOR Pro "Multipeak Fitting" operation. (D) The fitted peak could be decomposed into three Gaussian peaks (*cf.* Table 1), indicating polymorphism in the thin film. (E) Schematic depiction of a multilayer thin film, comprising stacked DOPC lamellar domains with the lattice plane of the bilayer (of spacing *d*) approximately parallel to the substrate. The lower limit of the domain size perpendicular to the lattice plane is indicated by the coherence length (L_a), obtained from the analysis of the broadening (as defined by the FWHM ΔQ) of the peaks in (D) using the Scherrer equation.

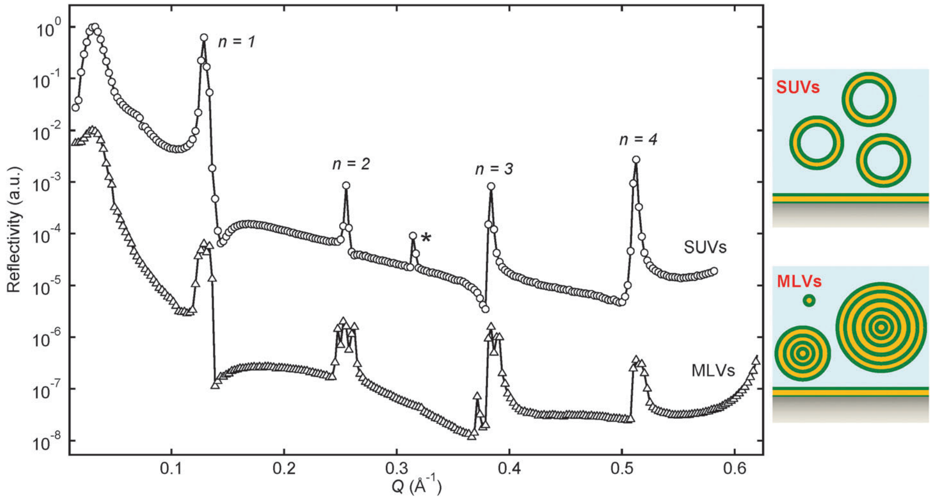

Fig. 3 XRR curves for DOPC multilayers on bare mica from an SUV (circles, top curve) and an MLV (triangles, bottom curve) dispersion. The peak (marked with *) at $Q \sim 0.32$ Å is the mica forbidden half Bragg peak.

Table 1 Peak position Q, the corresponding thickness d, and coherence length L_a for the DOPC multilayers from aqueous dispersions of MLVs. The polymorphism of MLV multilayers is evident from the presence of multiple peaks (denoted as $Q_{n,(1-4)}$) in the same order (n), and up to four d-spacing values were registered, albeit not all the constituent peaks could be resolved for the Bragg peaks due to insufficient angular resolution. Errors from the fittings are reported when they are greater than 0.5% for the Q values and greater than 0.1 Å for the d spacing values

DOPC dispersion MLVs				
	Diffraction order n (*cf.* Fig. 2)			
Parameter	1	2	3	4
$Q_{n,1}$ (Å^{-1})	0.125	0.247 ± 0.003	0.372	
d (Å)	50.1	50.9 ± 0.6	50.7 ± 0.1	
L_a (Å)	808.9 ± 50	3271.8 ± ~1000[a]	2408.6 ± 236.1	
$Q_{n,2}$ (Å^{-1})		0.253	0.383	0.511
d (Å)		49.6	49.2	49.1
L_a (Å)		1258.9 ± 33.5	1655.0 ± 49.3	2539.0 ± ~1000[a]
$Q_{n,3}$ (Å^{-1})	0.130	0.262	0.390	0.516
d (Å)	48.2	48.0	48.3	48.7
L_a (Å)	1199.4 ± 50	1676.6 ± 49.3	1348.1 ± 50.2	753.6 ± 38.1
$Q_{n,4}$ (Å^{-1})	0.135			
d (Å)	46.6			
L_a (Å)	2370.8			

[a] Large uncertainties due to a small number of fitted data points for the resolved peaks.

increase, a feature characteristic for XRR curves on mica due to the presence of mica's Bragg peak (Q = 0.64 Å^{-1}). Mica's forbidden half Bragg peak (Q = 0.32 Å^{-1}) is also present in some of the curves (always indicated with an asterisk (*)), which is due to mica's monoclinic unit cell encompassing two lattice layers.

Within a small Q range around the Bragg peaks, multiple peaks could be resolved, particularly pronounced for the n = 2, 3 peaks, revealing a complex structure of the sample. Here we focus on the analysis of the Bragg peaks using the Scherrer equation to yield the coherence length L_a, the physical meaning for which is the lower limit of the crystalline domain size perpendicular to the mica surface; it thus can be used as an indication of the structural order of the multilayer.[47,48] The analysis was performed in IGOR Pro as follows. As an example, for the 2nd order peak (n = 2) in Fig. 2A, the reflectivity data in the Q range (0.22–0.29 Å^{-1}) enclosing the peak was selected and the background reflectivity was fitted to a 4th order polynomial (*i.e.* $\sim Q^{-4}$; dotted black curve in Fig. 2B), and subtracted from the reflectivity data. The residual peak (circles in Fig. 2C) was subsequently fitted with the IGOR Pro "Multipeak Fitting" operation (black curve in Fig. 2C), which could be decomposed into three Gaussian profiles (Fig. 2D). As listed in Table 1, the peak positions Q for the three peaks (denoted as $Q_{n,(1-3)}$ for MLVs (n = 2); $Q_{2,1}$ = 0.247 Å^{-1}, $Q_{2,2}$ = 0.253 Å^{-1}, and $Q_{2,3}$ = 0.262 Å^{-1}) correspond to three d-spacing values (50.9 (±0.6), 49.6 and 48.0 Å respectively; for the last two d values the error from the fitting is less than 0.01 Å). Up to four d values were observed due to polymorphism, although not all the corresponding peaks could be resolved at each Bragg peak (*cf.* Table 1). At small Q the peaks overlap more, making it more difficult to resolve them. On the other hand, at very high Q the reflectivity is considerably diminished (as it scales $\sim Q^{-4}$), and this again could limit the resolution in de-convoluting the multiple peaks. Such a difference in d could be due to different lipid packing, arising from when the MLVs and other lipid aggregates ruptured to form multilayers. It could also be due to a slightly different residual water content in different domains, as the d-spacing of a DOPC multilayer has been observed to vary with the variation of humidity.[49]

The full width half maximum (Fig. 2(D); FWHM, ΔQ) values were also obtained from the analysis. The crystalline domain size (or coherence length, L_a, listed in Table 1) along the direction normal to the surface is inversely proportional to ΔQ and can be calculated using Scherrer's equation:[50]

$$L_a = \frac{2\pi K}{\Delta Q}, \qquad (2)$$

where K is the Scherrer constant, a shape factor ~1 (*e.g.* a common value is 0.94 for a cubic symmetry but it varies depending on the shape of the crystal and on how the width is determined). Then the number of bilayers m in the domain could be estimated as $m = L_a/d$.

In Fig. 3, XRR curves of the multilayers on mica obtained from drop casting of SUV and MLV dispersions are compared. In contrast to the MLV sample above, the Bragg peaks from the SUV sample are well defined single peaks, indicating that the multilayers were largely monomorphic with a constant d of 49.1 Å. The d values calculated from all the four orders of the Bragg peaks (*cf.* Table 2) are also in close agreement (the errors associated with d from each peak are smaller than 0.01 Å, and the average deviation from the mean value is 0.1 Å), further indicating well defined bilayer structures in the multilayer lamellae. In Table 3, the DOPC multilayer characteristics obtained for SUV and MLV samples are compared. The average domain size for the SUV sample in air (L_a = 1997.4 ± 27.2 Å) is much greater than that of the MLV sample (L_a = 1339.7 ± 59.0 Å, calculated as the average of the third peak of each diffraction order), and since the lattice spacing for the two samples is almost the same, it confirms a more ordered structure in the case of SUVs, the number of bilayers in the domain being ~41 for SUVs while only ~26 for MLVs. It is conceivable that monodispersed SUVs provided a more uniform structural template upon rupture, leading to a more organised structure; whereas the MLV dispersion consisted of a plethora of aggregates in the size range ~150–1500 nm, as revealed by DLS, which frustrated packing upon rupture at the interface, leading to both the polymorphic and less ordered structure observed.

Table 2 The bilayer thickness d, peak position Q_n, coherence length L_a, and the corresponding number of layers in the domain (m) for DOPC multilayers obtained from SUVs on bare mica in air. Errors for d and Q_n are <0.05% from the fitting

DOPC dispersion	SUVs			
Diffraction order n	Q_n (Å^{-1})	d (Å)	L_a (Å)	No. of layers m
1	0.128	49.1	1638.6 ± 31.8	34
2	0.255	49.3	2308.3 ± 26.4	47
3	0.384	49.1	2107.6 ± 33.0	43
4	0.512	49.1	1935.3 ± 17.6	39

Table 3 The bilayer thickness d, coherence length L_a, and the corresponding number of layers in the domain m for DOPC multilayers obtained from SUVs and MLVs on bare mica, in air and in water. Errors for d are <0.1% from the fitting

Condition	DOPC liposome dispersion	d (Å)	$L_a{}^a$ (Å)	No. of layers m
In air	SUVs	49.1	1997.4 ± 27.2	41
	MLVs	49.0	1435.8 ± 52.2	31
		48.3	1291.6 ± 62.5	26
Under water	SUVs	62.6	1078.3 ± 44.1	17
	MLVs	No Bragg peaks observed		

[a] Average values: for SUVs from all diffraction orders; for MLVs from the 2nd and 3rd resolved peaks in all diffraction orders (when present in air).

Fig. 4(A) indicates that drop cast DOPC multilayers formed on all the substrates. In the case of PEI-coated mica, the Bragg peaks are slightly broadened (L_a = 1323.4 ± 22.1 Å) compared to that of the bare mica sample (L_a = 1997.4 ± 27.2 Å), suggesting a slightly less ordered structure. The peaks are also shifted towards higher Q values, pointing to a slightly thinner bilayer (by ~3 Å), as compared to the multilayers on bare mica. All the samples were measured under the same ambient conditions, so it is unlikely that the structural differences were due to different relative humidity, and consequently different hydration, levels. PEI and mica would have exhibited different surface charge densities, and the interfacial roughness on PEI-coated mica is expected to be slightly higher. We thus attribute the observed structural differences to the interactions between the DOPC headgroups and the PEI layer. The dipole of the zwitterionic headgroup is oriented with the negative charge proximal, and the positive charge distal, to the tail. The outermost positive charge enables PC-lipids to attach to mica and to negatively charged polymers. In the case of the positively charged PEI-coated mica, the headgroups must adopt an orientation and arrangement different from that on bare mica (schematically shown in Fig. 4(B)), and this would consequently result in different lipid packing in the bilayer immediately adjacent to the surface. A thinner bilayer suggests that either tilting or interdigitation of the lipid tails occurred,[39] due to a slightly relaxed packing. It is curious and interesting that the Bragg peaks from the PEI-coated mica sample are monomorphic, which indicates that the surface bilayer had a templating effect and the bilayer packing was largely retained throughout the thin film.

In the case of more hydrophobic STAI-coated mica as the substrate, the DOPC multilayer thin film exhibited polymorphism, for instance with the two decomposed peaks from the n = 1 Bragg peak shown in the inset at the bottom left corner of Fig. 4, with the corresponding d-spacing and coherence length values of (d = 47.8 Å, L_a = 747.1 Å) and (d = 46.1 Å, L_a = 1603.6 Å) respectively (the errors in the thicknesses d, and full width at half maximum ΔQ, from the fitting is ~0 Å, thus the error on L_a is also almost null). That is, the film constituted domains with (at least) two different lattice spacing, and those with slightly thinner bilayers were more ordered. It is conceivable that, upon encountering the hydrophobic STAI monolayer, the DOPC SUVs

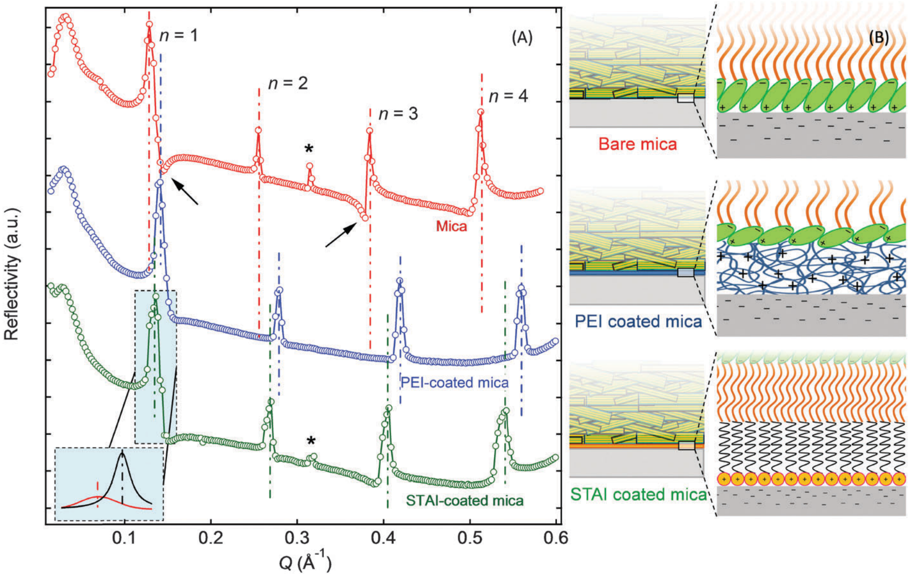

Fig. 4 (A) XRR curves for DOPC on bare mica, PEI-coated mica, and STAI coated mica collected in air at room temperature. The forbidden mica half Bragg peaks are indicated by *. The arrows indicate the presence of negative peaks, attributed to the relaxation of the top lipid layer at the air–film interface. The light blue rectangle shows the magnification of the fitting of the first Bragg peaks for the STAI-coated mica sample. (B) Schematic representation showing the three different substrates.

would rupture and also need to undergo cleavage so that the hydrophobic lipid tails are unzipped from the liposome bilayers, facing towards and in intimate contact with the STAI layer. The packing density of the tails would be influenced by that of the STAI monolayer and also the STAI surface coverage. Subsequent surface templating effects would lead to such bilayer structures being largely retained throughout the film.

A noticeable feature in the XRR curves of the SUV DOPC multilayer thin film on bare mica is the "negative" peaks, as indicated by two arrows in Fig. 4. As a detailed structural model shows,[51] this is due to the relaxation of the terminating monolayer at the air–film interface, most pronounced on bare mica and much less so on more hydrophobic STAI-coated mica and absent on PEI-coated mica.

It is known that lipid membranes are not stable under water[52] and bilayers tend to delaminate from lipid membranes.[32,37] It is important to understand the structural transition of lipid multilayers under water, a rapid process difficult to probe experimentally. Relatively fast XRR scans due to the high synchrotron X-ray flux have allowed us to compare the XRR curves of the DOPC multilayers from SUVs and MLVs at the initial stage of water submersion (Fig. 5). After 1 h under water, the Bragg peaks from the SUV DOPC multilayers shifted towards lower Q (Fig. 5B), consistent with thicker bilayers (d = 62.6 Å) due to the hydration of the headgroups. As compared to d = 49.1 Å in the ambient air, this represents bilayer swelling of $\Delta d \sim 13.5$ Å, corresponding to a hydration layer with 4–5 molecular water layers per bilayer. Similar swelling behaviour due to hydration has also been previously observed for supported purple membranes[53,54] using XRR. Furthermore, the Bragg peaks of hydrated samples are broader and less intense than those of dry multilayers, with an L_a = 1078.3 ± 44.1 Å as compared to L_a = 1997.4 ± 27.2 Å in air (*cf.* Table 3), and the 3rd and 4th Bragg peaks are also absent. The loss of crystalline long-range order is due to lattice defects and bending fluctuations in addition to water-induced bilayer undulations, which would also give rise to variations in the bilayer thickness. However, no significant peak splitting (*i.e.* polymorphism) was observed. These observations suggest that bilayer hydration occurred soon after water addition, and the swelling of the bilayers was largely uniform, with water molecules permeating through the multilayer structure. This resulted in swollen bilayers, with an overall less ordered multilayer structure. Our results from a separate experiment (Fig. S2 in the ESI†) show that the DOPC multilayer structure could be retained up to ∼2 h in water, where similar bilayer swelling was also observed.

Prolonged water submersion led to the loss of the multilayer structure, evident from the disappearance of the Bragg peaks (Fig. 5C; 2 h in water in this particular experiment). Instead, mild reflectivity oscillations called Kiessig fringes appear due to a lipid bilayer of thickness ∼45.3 Å remaining at the mica–water interface.[39] Detailed analysis of these Kiessig fringes requires the consideration of the crystal truncation rods of mica,[39,43] and will be presented in a further publication.[46]

For the DOPC multilayers prepared from a MLV dispersion, the Bragg peaks are absent in the XRR curve collected 20 min after water addition (Fig. 5D and E), suggesting a less stable film as compared to the SUV sample. Similarly, Kiessig fringes indicate the presence of a bilayer at the mica–water interface of thickness $d \sim 44.1$ Å,[46] in close agreement with that for the remnant bilayers in the SUV sample under water (∼45.3 Å). Our results indicate that, in addition to a more ordered structure, the multilayers from the SUV dispersion showed better stability against water, probably due to fewer structural defects where delamination of the multilayers would be initiated. We have

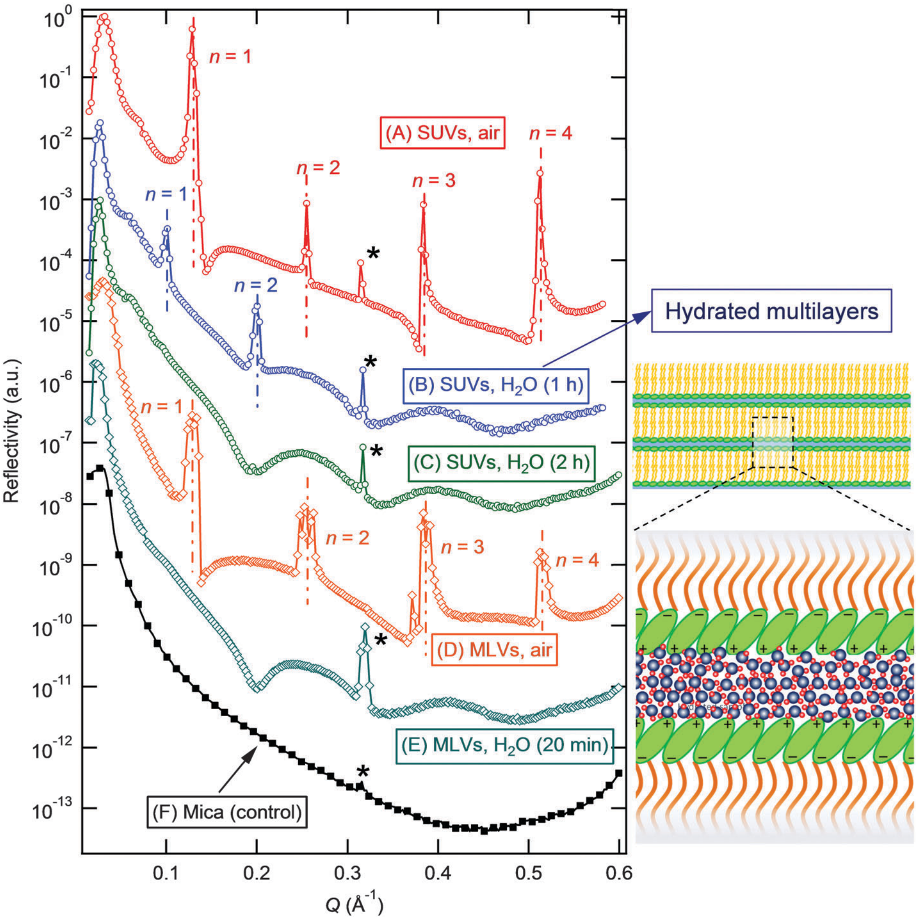

Fig. 5 XRR curves of SUV DOPC multilayers on mica in air (A), in water after 1 h (B) and 2 h immersion (C). XRR curves of MLV DOPC multilayers on mica in air (D), and in water after 20 min immersion (E). For comparison, the XRR curve of a control bare mica piece in air (*i.e.* without any DOPC layers) is shown in (F). The hydrated multilayers in the SUV sample under water (curve B) are shown schematically on the right hand side, with a hydration layer of thickness Δ*d* ∼ 13.5 Å per bilayer, corresponding to 4–5 molecular water layers.

also subsequently incubated the sample with a DOPC SUV dispersion; however, the multilayers were not re-formed in the solution (*cf.* Fig. S3D and E in the ESI†). In addition to the finite crystalline domain size as characterised by the coherence length L_a, the lattice spacing fluctuations (*i.e.* the paracrystalline disorder) may also contribute to the broadening of the Bragg peaks,[55] which is consequently accompanied by a decrease in the peak intensity. This originates from the crystallites with slightly different *d*-spacing values, manifesting in increased broadening of the Bragg peaks with increasing diffraction orders *n*. This is evident from the reduced L_a values in Table 1 for higher order peaks (n = 3, 4) in the case of SUV DOPC multilayers on mica. This means that the Scherrer equation is insufficient on its own to fully describe the structural order due to bilayer thickness fluctuations in the multilayer film, and a correction should be applied. The two contributions from the crystallite size and the distortion caused by the paracrystalline disorder may be separated by plotting the broadening of each peak ($(\Delta Q)^2/(2\pi)^2$) *versus* the fourth power of the diffraction order (h^4) for a plane of the Miller index ($h00$).[47,56,57] From the linear fit to the plot, $y = y_0 + mh^4$, the coherence length, L_a, and the degree of disorder in the crystal, g, can be inferred respectively from the intercept y_0 and the slope m as

$$g = \frac{1}{\pi}\left(md^2\right)^{1/4}, \tag{3}$$

and

$$L_a = (y_0)^{-1/2}. \tag{4}$$

Fig. 6 shows such a plot for the SUV DOPC multilayers in air on mica, PEI- and STAI-coated mica, as well as the MLV multilayer sample, for which at least three orders of reflections have been observed to allow this plot.[55] For SUV multilayers on mica, the bilayer thickness fluctuation is small and thus the slope of the plot is null ($m \sim 0$). The paracrystalline disorder parameter g (*cf.* Table 4) for the multilayer on the STAI-coated mica (0.0248 ± 0.0003) is greater than that for the PEI-coated sample (0.0177 ± 0.0007), and the MLV sample showed a degree of paracrystalline disorder (g = 0.0252 ± 0.0003) similar to that on STAI. The conclusion on the structural order from such an analysis thus concurs with that by the Scherrer equation analysis. The obtained L_a values, also listed in Table 4,

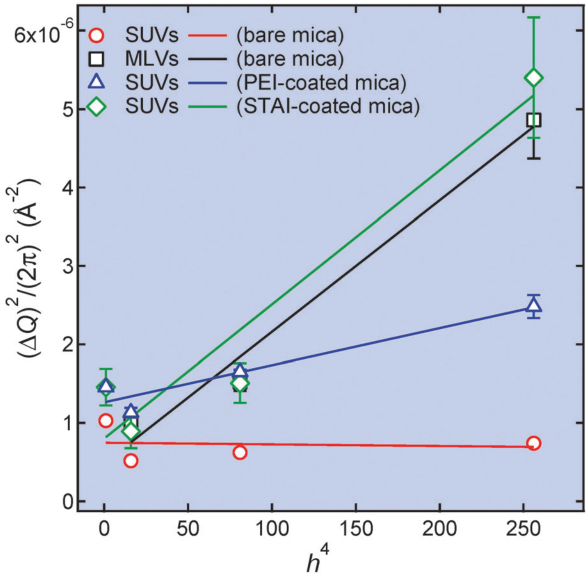

Fig. 6 Peak broadening $(\Delta Q)^2/(2\pi)^2$ of lamellar reflections as a function of the fourth power of the diffraction order h^4 for DOPC multilayers from MLVs on bare mica (squares), and SUVs on bare mica (circles), on PEI-coated mica (triangles), and STAI-coated mica (diamonds). From the slopes m of the linear fits ($y = y_0 + mx$), the paracrystalline disorder parameters g could be calculated from eqn (3). From the intercept y_0, the coherence length L_a could be estimated from eqn (4). These values are listed in Table 4. The error bars for the SUV multilayers on mica are smaller than the circles and thus invisible.

are comparable to those obtained from the Scherrer equation. Overall, the multilayers prepared from the SUV dispersions are more ordered than those from the MLVs, with larger crystalline domain sizes and smaller bilayer thickness perturbations. The values of number of layers m calculated using values obtained from eqn (3) and (4) are reported in Table 4, which are slightly higher than those obtained from the Scherrer equation, but follow the same trend.

4. Conclusions

In the present work, DOPC multilayers have been prepared by drop casting aqueous dispersions of liposomes on different substrates, and the multilayer structure has been studied using the synchrotron XRR technique, facilitated by a unique "bending mica" method.[43] In general, ordered lamellar structures consisting of DOPC bilayer domains have been obtained, with the lattice planes aligned approximately parallel to the substrate, evident from the distinct Bragg diffraction peaks in the XRR curve. The Bragg peaks have been analysed, using both the Scherrer equation and in terms of the degree of paracrystalline disorder, to yield detailed structural information. The multilayers prepared from monodispersed, well defined small unilamellar liposomes/vesicles (SUVs) ~90–100 nm in diameter were more ordered than those from multilamellar liposomes/vesicles (MLVs). This manifested as a larger coherence length (or domain size) perpendicular to the substrate, and an almost zero paracrystalline disorder parameter, which indicates little fluctuations in the bilayer thickness throughout the thin film. The MLV multilayers showed polymorphism, with multiple Bragg peaks observed, exhibiting a number of different bilayer thicknesses.

The SUV multilayers also showed stronger stability against water as compared to the MLV multilayers, retaining the Bragg peaks in water for up to 2 hours. This observation again points to a more ordered structure with fewer defects in the domains, where delamination of the multilayer would be initiated. Relatively fast XRR scans allowed us to study the rapid structural transition as the multilayers were submerged under water. We found that bilayers became swollen rapidly, with a hydration layer of thickness corresponding to 4–5 water molecular layers per bilayer.

We have also found that the surface chemistry of the substrate affected the multilayer structure. The multilayers cast on PEI- and STAI-coated mica from DOPC SUV dispersions had a higher degree of paracrystalline disorder than those on bare mica, with the STAI-coated mica, more hydrophobic compared to bare and PEI-coated mica, showing a greater effect, leading to structural polymorphism in the multilayers. This could be attributed to the interactions between the rupturing liposomes with the surface layer, dominating lipid packing immediately adjacent to the interface, which interestingly was templated by the bilayer domains subsequently formed, with the bilayer structure retained throughout the film. This highlights the importance of substrate chemistry, and conversely offers a mechanism to tune the multilayer structure by controlling the surface charge and wettability.

Table 4 Bilayer thickness d, coherence length L_a (from $n = 1$ Bragg peak), and the minimum number of bilayers m in the lamellae domain for SUV DOPC multilayers on bare, PEI- and STAI-coated mica. For comparison, the L_a and m values obtained from the paracrystalline disorder analysis are also reported. Errors for d are not reported as they are almost null (*i.e.* at least <0.05%) from the fitting

Substrate for SUV DOPC multilayers	d (Å)	L_a (Å)	No. of layers m	Paracrystalline disorder parameter g	L_a (Å) from Fig. 6 and eqn (4)	No. of layers m
Bare mica	49.1	1997.4 ± 27.2	41	~0	NA	NA
PEI-coated mica	45.0	1323.4 ± 22.1	29	0.0177 ± 0.0003	1480 ± 77	33
STAI-coated mica[a]	47.8	747.1 ± 10	16	NA	NA	NA
	46.1	1603.6 ± 10	35	0.0248 ± 0.0004	1854 ± 523	40
MLV DOPC multilayers on bare mica[b]	48.3	1259.4 ± 41.9	26	0.0252 ± 0.0003	1581 ± 384	33

[a] Values correspond to the two decomposed peaks (*cf.* Fig. 4A). [b] Multiple peaks are present for each Bragg peak due to polymorphism but not all resolved at each Bragg peak; here the third peak ($Q_{n,3}$) of the decomposed peaks from $n = 1$, 2, 3, and 4 Bragg peaks in the XRR curve for the MLV DOPC multilayer sample is used, which has also allowed the paracrystalline disorder parameter g (Fig. 6) to be extracted.

Previously, lipid multilayers have been typically prepared from an organic solvent, due to the extremely low solubility of lipids in water. We suggest that DOPC liposomes serve a dual role. They act as a delivery matrix – here an appreciable lipid concentration in water (up to ~25 mg mL^{-1} or 14 mM) was feasible. In addition, they serve as a structural precursor, with their lamellar structure readily retained upon rupture at the solid surface upon evaporation to facilitate rapid multilayer formation. Pre-forming such liposomes in aqueous media would also offer a mechanism to incorporate desired functional ingredients in the lamellar structure, which could be readily transferred to the multilayers. Other potential variables such as controlling the evaporation rate *via* temperature and using solvent mixtures could offer further mechanisms for tailoring the multilayer structure and await future exploitation. Our results represent first detailed structural characterisation of lipid multilayers *via* the pathway of drop casting aqueous liposome dispersions, pointing to the controlled preparation of ordered lipid multilayers by tailoring the liposome homogeneity and substrate surface properties, potentially offering a simple method for the inclusion of hydrophilic and hydrophobic functional additives (*e.g.* drugs or nanoparticles; Sironi *et al.*, in preparation[46]) in lipid multilayer based hybrid materials.

Acknowledgements

We would like to acknowledge funding from the Engineering and Physical Science Research Council (EPSRC), the Royal Society, the European Research Council (ERC, Advanced Grant HydrationLube, awarded to J. K.), Taiho Kogyo Tribology Research Foundation (TTRF), the European Cooperation in Science and Technology (CMST COST) Action CM1101, and the Marie Curie Initial Training Network (MC-ITN) NanoS3. We also thank the European Synchrotron Radiation Source (ESRF) and Diamond Light Source (Expt. number SI13139) for access to synchrotron X-ray sources. The XMaS-BM28 beamline is a mid-range facility supported by EPSRC, and we are grateful to all the beam line team staff for their support. XRR data extraction was performed using an Igor Pro software package developed by T. Dane (presently at ESRF). A. S. and T. S. were supported by EPSRC CASE Awards, and C. R. by an Everett Scholarship.

Notes and references

1 P. Mueller, H. T. Tien, W. C. Wescott and D. O. Rudin, *Circulation*, 1962, **26**, 1167–1171.
2 L. K. Tamm and H. M. McConnell, *Biophys. J.*, 1985, **47**, 105–113.
3 M. Eeman and M. Deleu, *Biotechnol., Agron., Soc. Environ.*, 2010, **14**, 719–736.
4 M. Mazzon and J. Mercer, *Cell. Microbiol.*, 2014, **16**, 1493–1502.
5 G. Bilek, N. M. Matscheko, A. Pickl-Herk, V. U. Weiss, X. Subirats, E. Kenndler and D. Blaas, *J. Virol.*, 2011, **85**, 8368–8375.
6 K. Simons and D. Toomre, *Nat. Rev. Mol. Cell Biol.*, 2000, **1**, 31–39.
7 J. A. Allen, R. A. Halverson-Tamboli and M. M. Rasenick, *Nat. Rev. Neurosci.*, 2007, **8**, 128–140.
8 T. Yang, O. K. Baryshnikova, H. Mao, M. A. Holden and P. S. Cremer, *J. Am. Chem. Soc.*, 2003, **125**, 4779–4784.
9 H. Jung, A. D. Robison and P. S. Cremer, *J. Struct. Biol.*, 2009, **168**, 90–94.
10 M. Gavutis, S. Lata, P. Lamken, P. Müller and J. Piehler, *Biophys. J.*, 2005, **88**, 4289–4302.
11 S. Majd and M. Mayer, *Angew. Chem.*, 2005, **117**, 6855–6858.
12 A. P. Quist, E. Pavlovic and S. Oscarsson, *Anal. Bioanal. Chem.*, 2005, **381**, 591–600.
13 J. Chalmeau, C. le Grimellec, J. Sternick and C. Vieu, *Colloids Surf., B*, 2012, **89**, 188–195.
14 C. K. Yee, M. L. Amweg and A. N. Parikh, *Adv. Mater.*, 2004, **16**, 1184–1189.
15 J. A. Jackman, W. Knoll and N.-J. Cho, *Materials*, 2012, **5**, 2637–2657.
16 E. T. Castellana and P. S. Cremer, *Surf. Sci. Rep.*, 2006, **61**, 429–444.
17 Y. K. Lee, H. Lee and J.-M. Nam, *NPG Asia Mater.*, 2013, **5**, e48.
18 A. E. Kusi-Appiah, N. Vafai, P. J. Cranfill, M. W. Davidson and S. Lenhert, *Biomaterials*, 2012, **33**, 4187–4194.
19 O. A. Nafday and S. Lenhert, *Nanotechnology*, 2011, **22**, 1–7.
20 O. A. Nafday, T. W. Lowry and S. Lenhert, *Small*, 2012, **8**, 1021–1028.
21 S. Lenhert, F. Brinkmann, T. Laue, S. Walheim, C. Vannahme, S. Klinkhammer, M. Xu, S. Sekula, T. Mappes, T. Schimmel and H. Fuchs, *Nat. Nanotechnol.*, 2010, **5**, 275–279.
22 S. Lenhert, P. Sun, Y. Wang, H. Fuchs and C. A. Mirkin, *Small*, 2007, **3**, 71–75.
23 L. Tayebi, Y. Ma, D. Vashaee, G. Chen, S. K. Sinha and A. N. Parikh, *Nat. Mater.*, 2012, **11**, 1074–1080.
24 R. Caminiti, G. Caracciolo, M. Pisani and P. Bruni, *Chem. Phys. Lett.*, 2005, **409**, 331–336.
25 D. Constantin, C. Ollinger, M. Vogel and T. Salditt, *Eur. Phys. J. E: Soft Matter Biol. Phys.*, 2005, **18**, 273–278.
26 L. P. Cavalcanti, H. Haas, H. N. Bordallo, O. Konovalov, T. Gutberlet and G. Fragneto, *Eur. Phys. J.: Spec. Top.*, 2007, **141**, 217–221.
27 H. Y. Jing, D. H. Hong, B. D. Kwak, D. J. Choi, K. Shin, C. J. Yu, J. W. Kim, D. Y. Noh and Y. S. Seo, *Langmuir*, 2009, **25**, 4198–4202.
28 T. Salditt, C. Li, A. Spaar and U. Mennicke, *Eur. Phys. J. E: Soft Matter Biol. Phys.*, 2002, **7**, 105–116.
29 M. Vogel, C. Münster, W. Fenzl and T. Salditt, *Phys. Rev. Lett.*, 2000, **84**, 390–393.
30 M. Seul and M. J. Sammon, *Thin Solid Films*, 1990, **185**, 287–305.
31 U. Mennicke and T. Salditt, *Langmuir*, 2002, **18**, 8172–8177.
32 L. Perino-Gallice, G. Fragneto, U. Mennicke, T. Salditt and F. Rieutord, *Eur. Phys. J. E: Soft Matter Biol. Phys.*, 2002, **8**, 275–282.
33 T. Salditt, C. Munster, J. Lu, M. Vogel, W. Fenzl and A. Souvorov, *Phys. Rev. E: Stat. Phys., Plasmas, Fluids, Relat. Interdiscip. Top.*, 1999, **60**, 7285–7289.

34 C. Munster, T. Salditt, M. Vogel, R. Siebrecht and J. Peisl, *Europhys. Lett.*, 1999, **46**, 486–492.

35 T. Salditt, *J. Phys.: Condens. Matter*, 2005, **17**, R287.

36 S. Tristram-Nagle, in *Methods in Membrane Lipids*, ed. A. Dopico, Humana Press, 2007, ch. 5, vol. 400, pp. 63–75.

37 A. C. Simonsen and L. A. Bagatolli, *Langmuir*, 2004, **20**, 9720–9728.

38 M. C. Duff, *Am. Mineral.*, 2004, **89**, 254.

39 F. Speranza, G. A. Pilkington, T. G. Dane, P. T. Cresswell, P. Li, R. M. J. Jacobs, T. Arnold, L. Bouchenoire, R. K. Thomas and W. H. Briscoe, *Soft Matter*, 2013, **9**, 7028–7041.

40 W. H. Briscoe, M. Chen, I. E. Dunlop, J. Klein, J. Penfold and R. M. J. Jacobs, *J. Colloid Interface Sci.*, 2007, **306**, 459–463.

41 K. L. Browning, L. R. Griffin, P. Gutfreund, R. D. Barker, L. A. Clifton, A. Hughes and S. M. Clarke, *J. Appl. Crystallogr.*, 2014, **47**, 1638–1646.

42 G. Silbert, J. Klein and S. Perkin, *Faraday Discuss.*, 2010, **146**, 309–324.

43 W. H. Briscoe, F. Speranza, P. X. Li, O. Konovalov, L. Bouchenoire, J. van Stam, J. Klein, R. M. J. Jacobs and R. K. Thomas, *Soft Matter*, 2012, **8**, 5055–5068.

44 M. J. Hope, M. B. Bally, L. D. Mayer, A. S. Janoff and P. R. Cullis, *Chem. Phys. Lipids*, 1986, **40**, 89–107.

45 A. Jesorka and O. Orwar, *Annu. Rev. Anal. Chem.*, 2008, **1**, 801–832.

46 B. Sironi, T. Snow, C. Redeker, J. Bartenstain, O. Bikondoa, J. Klein and W. H. Briscoe, *in preparation*.

47 T. G. Dane, P. T. Cresswell, O. Bikondoa, G. E. Newby, T. Arnold, C. F. J. Faul and W. H. Briscoe, *Soft Matter*, 2012, **8**, 2824–2832.

48 P. Scherrer, *Gottinger Nachrichten Gesell*, 1918, **2**, 98.

49 Y. Ma, S. K. Ghosh, S. Bera, Z. Jiang, S. Tristram-Nagle, L. B. Lurio and S. K. Sinha, *Phys. Chem. Chem. Phys.*, 2015, **17**, 3570–3576.

50 A. L. Patterson, *Phys. Rev.*, 1939, **56**, 978–982.

51 B. Sironi, T. Snow, J. Klein and W. H. Briscoe, 2016, *in preparation*.

52 G. Gupta, S. Iyer, K. Leasure, N. Virdone, A. M. Dattelbaum, P. B. Atanassov and G. P. López, *ACS Nano*, 2013, **7**, 5300–5307.

53 N. H. M. Kaus, A. M. Collins, O. Bikondoa, P. T. Cresswell, J. M. Bulpett, W. H. Briscoe and S. Mann, *J. Mater. Chem. C*, 2014, **2**, 5447–5452.

54 A. M. Collins, N. H. Mohd Kaus, F. Speranza, W. H. Briscoe, D. Rhinow, N. Hampp and S. Mann, *J. Mater. Chem.*, 2010, **20**, 9037–9041.

55 R. Hosemann and A. M. Hindeleh, *J. Macromol. Sci., Part B: Phys.*, 1995, **34**, 327–356.

56 T. G. Dane, P. T. Cresswell, G. A. Pilkington, S. Lilliu, J. E. Macdonald, S. W. Prescott, O. Bikondoa, C. F. J. Faul and W. H. Briscoe, *Soft Matter*, 2013, **9**, 10501–10511.

57 S. Lilliu, T. Agostinelli, E. Pires, M. Hampton, J. Nelson and J. E. Macdonald, *Macromolecules*, 2011, **44**, 2725–2734.